FORMATION OF CALCIUM H AND K GRAINS

Mats Carlsson
Institute of Theoretical Astrophysics, P.O. Box 1029, Blindern, N–0315 Oslo, Norway

AND

Robert F. Stein
Department of Physics & Astronomy, Michigan State University, East Lansing, MI 48824, USA

ABSTRACT

We have simulated the generation of Ca II H_{2V} bright grains by acoustic shocks. We employ a one-dimensional, non-LTE, radiation hydrodynamic code, with 6 level model atoms for hydrogen and singly ionized calcium. We drive acoustic waves through a stratified radiative equilibrium atmosphere by a piston, whose velocity is chosen to match the Doppler shift observed in the FeI λ 396.68 line in the H line wing, formed at about 260 km above $\tau_{500} = 1$.

The simulations closely match the observed behavior of Ca II H_{2V} bright grains down to the level of individual grains. The bright grains are produced by shocks near 1 Mm above τ_{500}=1. Shocks in the mid chromosphere produce a large source function (and therefore high emissivity) because the density is high enough for collisions to couple the Ca II populations to the local conditions. The asymmetry of the line profile is due to velocity gradients near 1 Mm. Material motion Doppler shifts the frequency where atoms emit and absorb photons, so the maximum opacity is located at – and the absorption profile is symmetric about – the local fluid velocity, which is shifted to the blue behind shocks. The optical depth depends on the velocity structure higher up. Shocks propagate generally into downflowing material, so there is little matter above to absorb the Doppler shifted radiation. The corresponding red peak is absent because of small opacity at the source function maximum and large optical depth due to overlying material. The bright grains are produced primarily by waves from the photosphere that are slightly above the acoustic cutoff frequency. The precise time and strength of a grain depends on the interference between these waves near the acoustic cutoff frequency and higher frequency waves. When waves near the acoustic cutoff frequency are weak, then higher frequency waves may produce grains. The "five-minute" trapped p-mode oscillations are not the source of the grains, although they can slightly modify the behavior of higher frequency waves.

Subject headings: hydrodynamics – radiative transfer – shock waves – Sun:chromosphere

1. INTRODUCTION

The solar atmosphere is a dynamic radiating medium. Many of its outstanding problems require consideration of the coupling between hydrodynamics, thermodynamics and radiation for their understanding. Detailed comparison of the evolution of line profiles observed with high spatial and temporal resolution with self-consistent radiation-hydrodynamic simulations provides diagnostics for atmospheric dynamics.

We have developed a code that is capable of such a self-consistent radiation-hydrodynamic treatment under solar chromospheric conditions with the important radiative transitions treated in non-LTE. In a previous papers we showed that the enhanced chromospheric emission, which corresponds to an outwardly increasing semi-empirical temperature structure, can be produced by acoustic waves without any increase in the mean gas temperature (Carlsson & Stein 1995). In this paper, we focus on the behavior of the Ca II line profiles because high quality data are available, they are the only resonance lines of a majority species formed at chromospheric heights in the visible part of the spectrum, and the question of what drives the appearance of K_{2V} bright grains has been much debated (e.g. Rutten & Uitenbroek 1991 and references therein, Rammacher & Ulmschneider 1992, Rossi et al. 1992, Von Uexkuell & Kneer 1995, Hofmann et al. 1996, Steffens et al. 1996, Kalkofen 1996).

We describe our methodology in section 2 and present the results on the formation of H_{2V} and K_{2V} bright grains in section 3. The limitations of our calculations are discussed in section 4 and our conclusions are summarized in section 5.

2. METHOD

2.1. *The Computation*

We solve the one-dimensional equations of mass, momentum, energy and charge conservation together with the non-LTE radiative transfer and population rate equations, implicitly on an adaptive mesh. The advection terms are treated using Van Leer's (1977) second order upwind scheme to ensure stability and monotonicity in the presence of shocks. An adaptive mesh is used (Dorfi & Drury 1987) in order to resolve the regions where the fluid properties are changing rapidly (such as in shock fronts). The radiative transfer is treated using Scharmer's method (Scharmer 1981, Scharmer & Carlsson 1985, Carlsson 1986). We employ 6 level model atoms for hydrogen and singly ionized calcium. Other continua are treated as background continua in LTE, using the Uppsala atmospheres program (Gustafsson 1973). Microturbulence broadening was set to a constant 2 km/s throughout the atmosphere. The equations are solved implicitly to ensure stability in the presence of radiative energy transfer, and to have the time steps controlled by the rate of change of the variables and not by the Courant time for the smallest zones. There is a transmitting boundary condition at the top of the computational domain.

2.2. Initial Atmosphere

Our initial atmosphere (Fig. 1) is in radiative equilibrium above the convection zone (for the processes we consider) without line blanketing and extends 100 km into the convection zone, with a time constant divergence of the convective energy flux (on a column mass scale) calculated with the Uppsala code without line blanketing.

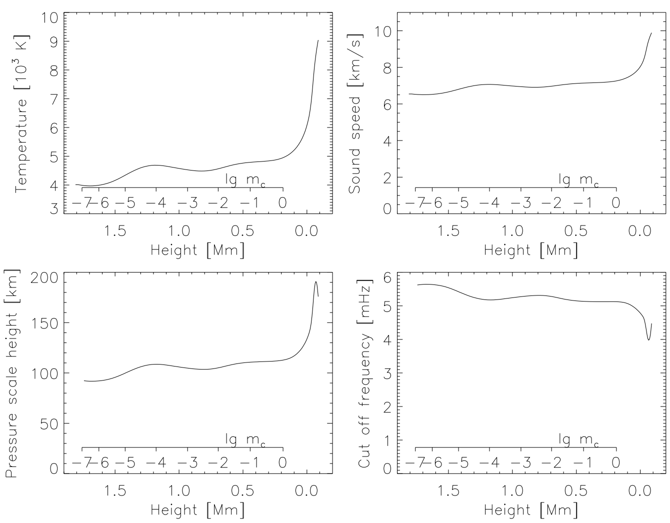

Fig. 1. Temperature, sound speed, pressure scale height and acoustic cut off frequency as functions of height in the starting atmosphere. lg(column mass) is given as a secondary scale.

2.3. Driving

Waves are driven through the atmosphere by a piston located at the bottom of the computational domain (100 km below $\tau_{500} = 1$). The piston velocity is chosen to reproduce a 3750 second sequence of Doppler shift observations in an Fe I line at λ396.68 nm in the wing of the Ca II H-line (Lites et al. 1993). We calculated the transfer function for the velocity between the piston and 260 km above $\tau_{500} = 1$ (the height of formation of the iron line),

$$F[v_{260\,\mathrm{km}}] = HF[v_{\mathrm{piston}}], \tag{1}$$

where $F[v_{260\,\mathrm{km}}]$ denotes the Fourier transform of the velocity at a height of 260 km. The piston velocities are then obtained as

$$v_{\mathrm{piston}} = F^{-1}(H^{-1}F(v_{\mathrm{Fe}})). \tag{2}$$

Here v_{Fe} is the observed Doppler shift in the λ396.68 nm Fe I line and v_{piston} is the piston velocity.

The velocity spectrum as a function of frequency changes with height, both in amplitude and phase. The velocity amplitude of propagating waves increases with height in a stratified atmosphere to maintain a constant flux as the density decreases. Damping reduces this amplitude increase. Propagating modes also show a phase shift due to their finite phase speed. Evanescent modes are attenuated but have no change in phase as a function of height. The transfer function is thus a complex valued function where the absolute value gives the ratio of velocity amplitude between the two heights and the phase gives the $(v_{z_2} - v_{z_1})$ phase difference.

The transfer function from the height of the piston to the formation height of the Fe I line at λ396.68 nm (about 260 km) is shown in Fig. 2. The phase difference shows the expected behavior. There is no phase difference in the evanescent regime below the cut-off frequency (which varies from 4 mHz at the bottom to 5 mHz at 300 km height, see Fig.1). The phase difference for propagating waves becomes increasingly negative for larger frequencies, asymptotically approaching $\Delta\phi = -\omega\Delta z/v_{\mathrm{sound}}$. The velocity amplitude in the evanescent regime is nearly constant with height indicating strong damping, since for undamped waves the amplification factor would be $\exp(\Delta z/2H) = 2.6$–5.1 over 360 km with a pressure scale height of 110–190 km. For propagating frequencies, the amplification approaches the undamped value. At higher fre-

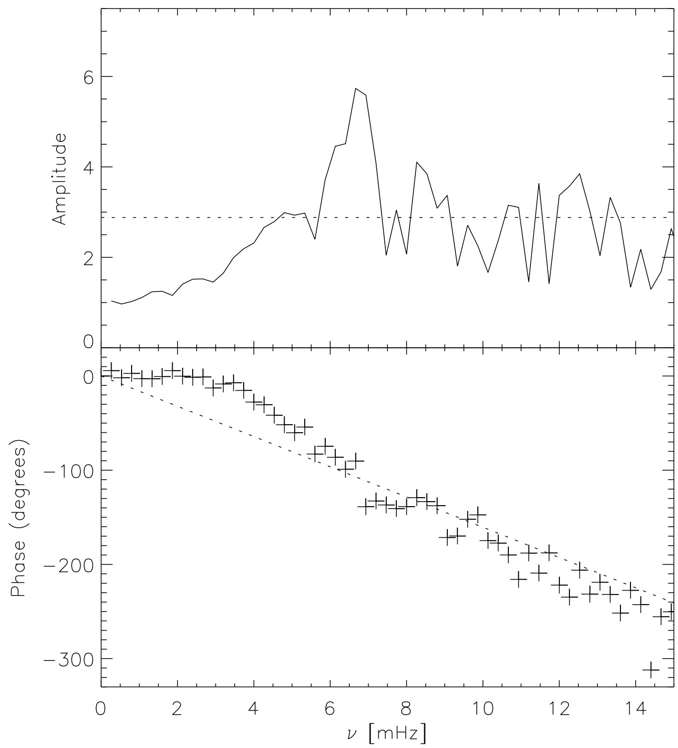

Fig. 2. Velocity transfer function from the height of the piston to the formation height of the observed Fe I line at λ396.68 nm (about 260 km) with velocity amplification in the top panel (dotted line: undamped amplification factor of $\exp(\Delta z/2H)$, and phase shift in the bottom panel. The dotted line in the bottom panel shows the asymptotic phase relations $\Delta\phi = -\omega\Delta z/v_{\mathrm{sound}}$.

quencies the amplitude and phase of the transfer function become ill determined because of low driving power.

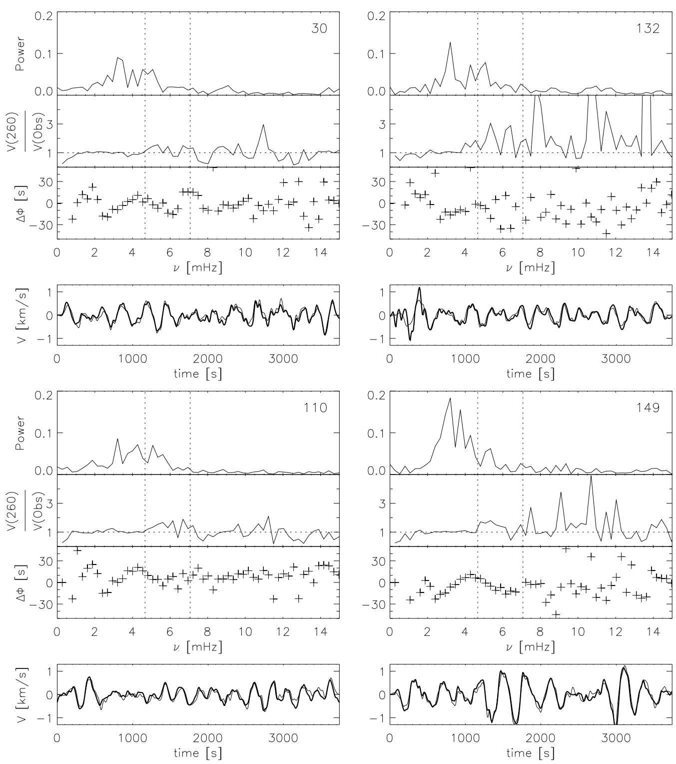

Fig. 3. Velocity power in the simulation at a height of 260 km above $\tau_{500} = 1$ and a comparison of the simulated velocity with the observed Doppler velocities in the λ396.68 nm Fe I line. The comparison shows the ratio of amplitudes ($V_{260\,\mathrm{km}}/V_{\mathrm{obs}}$) and the differences in phase ($V_{260\,\mathrm{km}} - V_{\mathrm{obs}}$) (negative phase difference means the simulated velocity lags the observed one) as a function of frequency and in the bottom panel the velocities are compared as a function of time (the heavy line is the simulation and the light line is the observed velocity). The vertical dotted lines at 4.7 and 7.1 mHz mark the boundaries of the low, medium and high frequency ranges discussed later. Results at four different slit positions are shown.

This transfer function was then used to compute piston velocities from the observed iron line Doppler shifts at four positions along the slit. The simulated velocity field at a height of 260 km is compared with the observed Doppler shifts in Fig. 3. All four cases show similar behavior. There is too little power in the simulation at the very lowest frequencies (< 0.5 mHz). Throughout the evanescent band (0 - 5 mHz) the amplitude ratio is close to one and the phase difference close to 0^o. There is slightly too much power in the simulation velocities in the intermediate frequency band (4.7 - 7.1 mHz) and the simulated velocities lag the observed Doppler shifts (negative phase differences). In the high frequency band (> 7.1 mHz), there is little power and the amplitude ratios and phase differences show large variations. Note that the match between simulation and observation is significantly worse for slit position 132 than the other cases. Also, note that there is much more low frequency power at slit position 149 than in the other cases. Generally, in the intermediate frequency band, there is maximum power at 5 mHz and the power decreases with increasing frequency.

The velocity amplitude at 260 km height is about 10% of the local sound speed. Higher up in the atmosphere we would expect the concept of a transfer function as a property of the atmosphere to break down because the large amplitude perturbations modify the atmosphere significantly.

3. RESULTS

The quasi-periodic emission in the core of the H and K lines of ionized calcium is asymmetric with often strong emission on the violet side of the line center (so called H_{2V} and K_{2V} bright grains) and seldom any emission on the red side. In this section we show that these bright grains are produced by acoustic shocks in the mid-chromosphere. Their asymmetric appearance is due to the large velocity gradient in the shocks, which shifts the absorption and emission profiles of the material behind the shock to the blue, where there is little opacity above the shock. We reveal that the occurrence of grains is entirely determined by the photospheric velocity field, primarily waves near the acoustic cutoff period ($\approx$ 3 min) interacting with higher frequency waves. Finally, we compare our simulation results with observations. The appearance of grains in the simulations generally matches the observations, down to the occurrence of individual grains.

3.1. Formation of emergent H-line intensity

The emergent intensity is given by the formal solution of the transfer equation:

$$I_\nu = \int_{z0}^{z1} S_\nu e^{-\tau_\nu} \chi_\nu dz. \tag{3}$$

The intensity contribution function is composed of the source function, S_ν, an exponential attenuation factor ($e^{-\tau_\nu}$) and the product of the cross–section and the column density of emitters $\chi_\nu dz$, where $\chi_\nu \equiv \sum_i n_i \sigma_{i\nu}$ is the monochromatic opacity per volume and thus a measure of the density of emitting particles. This formal solution can be rewritten as:

$$I_\nu = \int_{z0}^{z1} S_\nu \tau_\nu e^{-\tau_\nu} \frac{\chi_\nu}{\tau_\nu} dz. \tag{4}$$

The optical depth factors have been reorganized as: $\tau_\nu e^{-\tau_\nu}$ which has a sharp peak at $\tau_\nu = 1$ and χ_ν/τ_ν which is important when there are many emitting particles (large χ_ν) at small optical depth (small τ_ν). A brightening on the blue side of the line is produced when all three factors are large at a frequency blue shifted from line center.

A large source function, S_ν, (independent of frequency across the central part of the line because we assume complete redistribution, CRD) is produced when a strong wave or shock produces a high temperature at an altitude of about 1 Mm where the density is large enough for the source function to be significantly coupled to the Planck function. Above this height, the source function becomes increasingly decoupled from the Planck function and responds less to the presence of a shock. Below this height the waves are weaker and produce less enhancement in the source function.

The factor $\tau_\nu e^{-\tau_\nu}$ is large where the optical depth $\tau_\nu = 1$. The height where this occurs decreases with increasing offset from the line center.

The factor responsible for the asymmetry of the Ca II lines is χ_ν/τ_ν, which is large where the opacity χ_ν is large at small optical depth τ_ν, a situation that typically arises in the presence of strong velocity gradients. Material motion Doppler shifts the frequency where atoms emit and absorb photons, so the maximum opacity is located at – and the absorption profile is symmetric about – the local fluid velocity. The optical depth depends on the velocity structure higher up, i.e. on the velocity gradients. Where the velocity decreases inward (upward velocity positive), higher lying atoms absorb at bluer wavelengths, so the opacity higher up is smaller on the red side of the line and χ_ν/τ_ν is larger toward the red of the velocity. Where the velocity increases inward, higher lying atoms absorb at redder wavelengths, so the opacity higher up is smaller on the blue side of the line and χ_ν/τ_ν is larger toward the blue of the velocity. Upward propagating shocks generally accelerate atoms upward into downward moving fluid. Hence, above a shock there is little contribution to the optical depth on the blue side and a large contribution to the optical depth on the red side of the line. As a result, this asymmetry factor is large on the blue and small on the red side of lines at shocks. The magnitude of this effect depends on the magnitude of the velocity gradient – that is the strength of the wave or shock.

To get an asymmetric profile with no red peak thus requires a large velocity gradient at a low enough height that significant numbers of atoms are present. The position of the violet peak is set by the amplitude of the shock and the width of the absorption profile. The brightness of the peak is set by the shock formation height – lower height produce brighter peaks due to the stronger coupling of the source function to the temperature increase in the shock at lower altitudes.

The formation of the H_{2V} bright grains is shown in the following series of figures (Figs. 4–7) in the form of the contribution function to intensity and the factors that contribute to it. Each figure has four panels with the full contribution function in the lower right panel and its three factors in the three other panels. The functions are shown as grey-scale images as functions of frequency in the line (in velocity units) and height in the atmosphere. The image in the lower right panel is thus the product of the three other images. All panels also show the velocity as a function of height (with upward velocity positive to the left in the figure) and the height where $\tau_\nu = 1$ (grey line). The top right panel, in addition, shows the Planck function (dotted) and the source function (dashed) with high values to the left. The bottom right panel also shows the emergent intensity as a function of frequency. The time in seconds from the start of the simulation is shown in the top left panel.

Figure 4 shows the situation at the start of the simulation before any waves have traveled through the atmosphere. The atmosphere is static and the velocity is zero everywhere. The emergent intensity (lower right panel) shows no emission. Optical depth unity (all panels) occurs at 1.65 Mm at line center and at lower heights further out from the center. Its shape follows the atomic absorption profile, with a Doppler core within ±7.5 km/s and Lorentzian damping wings farther out. All factors entering the calculation of the contribution function are symmetric with respect to line center.

Figure 5 shows the situation after 650 seconds. Several shocks have traveled through the atmosphere and there is now a shock at 1.4 Mm with two waves behind it that are steepening. The source function (upper right image and dashed line) has

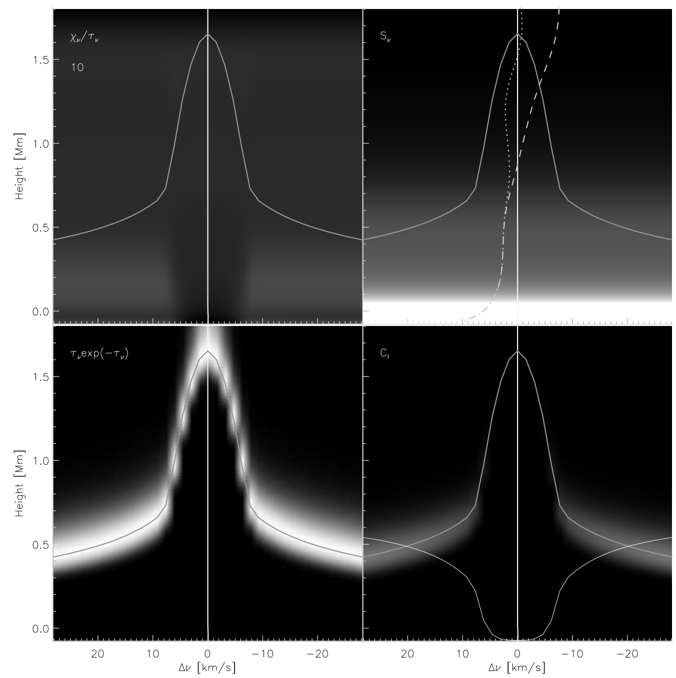

Fig. 4. The formation of the H_{2V} bright grains – images of the contribution function to intensity (lower right) and the factors entering its calculation, χ_ν/τ_ν (upper left), S_ν (upper right) and $\tau_\nu \exp(-\tau_\nu)$ (lower left). The functions are shown as grey-scale images as functions of frequency in the line (in velocity units) and height in the atmosphere. All panels also show the velocity as a function of height (with upward velocity positive to the left in the figure) and the height where $\tau_\nu = 1$ (grey line). The top right panel, in addition, shows the Planck function (dotted) and the source function (dashed), with high values to the left. The source function (image, upper right panel) is constant across the line at a given height, because of the assumption of CRD, and is substantially below the Planck function above 1 Mm due to the non-LTE decoupling. The bottom right panel also shows the emergent intensity as a function of frequency. The time in seconds from the start of the simulation is shown in the top left panel.

a maximum at the wave at 0.8 Mm, where the temperature increase occurs at sufficiently high density for collisions to couple the populations to the local state of the gas. It is independent of frequency across the line, because we assumed complete redistribution. The source function is substantially smaller than the Planck function (dotted line) behind the shock and larger than the Planck function ahead of the shock due to the non-LTE decoupling. The $\tau_\nu e^{-\tau_\nu}$ factor gives weight around $\tau_\nu = 1$ (lower left panel). The absorption profile is now shifted by the fluid velocity which produces the asymmetric shape of the optical depth unity curve. The χ_ν/τ_ν factor gives weight to those frequencies and depths where a velocity gradient produces large opacity at small optical depth (upper left panel). From the top of the computational domain down to the shock at 1.4 Mm the velocity decreases. Above a given point there is thus more absorption and therefore larger optical depth on the blue side than on the red side. Hence, the χ_ν/τ_ν factor is largest toward the red of the velocity. At the shock at 1.4 Mm and the waves at 1.2 and 0.8 Mm the velocity increases downwards. Here there is more absorption by overlying material to the red of the velocity

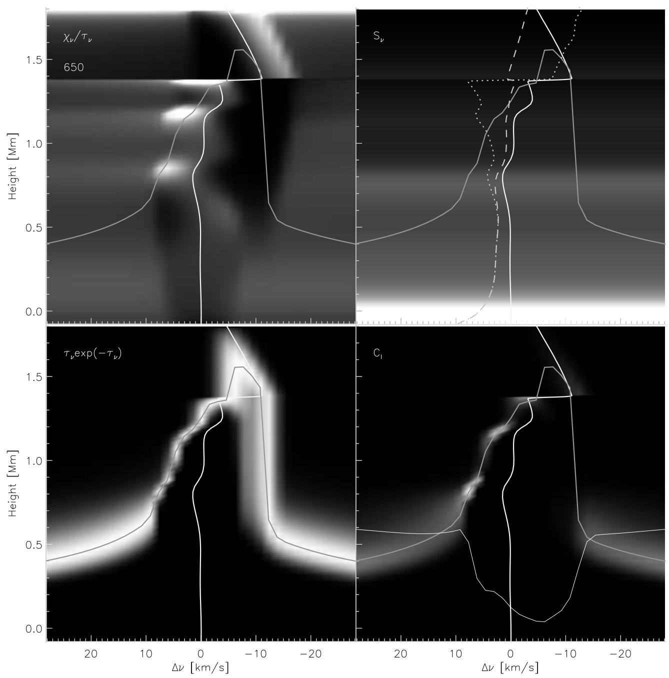

Fig. 5. As Fig. 4 but for t=650s.

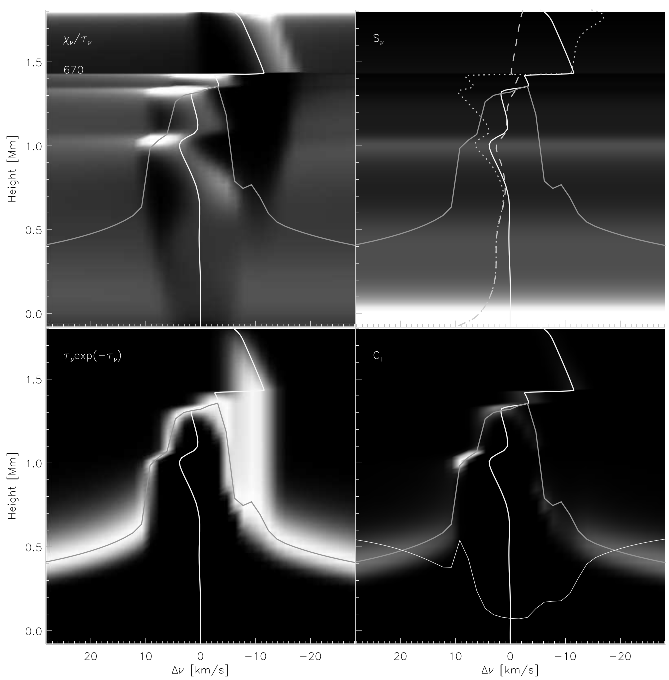

Fig. 6. As Fig. 4 but for t=670s.

and the maximum of the χ_ν/τ_ν factor occurs toward the blue of the velocity. The factor is largest at 1.4 Mm because of the large velocity gradient in the shock and the large amplitude of the velocity jump across the shock. The smallness of the χ_ν/τ_ν factor below 1.4 Mm at unit optical depth on the red side of the line at -12 km/s is caused by the small opacity (large displacement from the material velocity) and the large optical depth

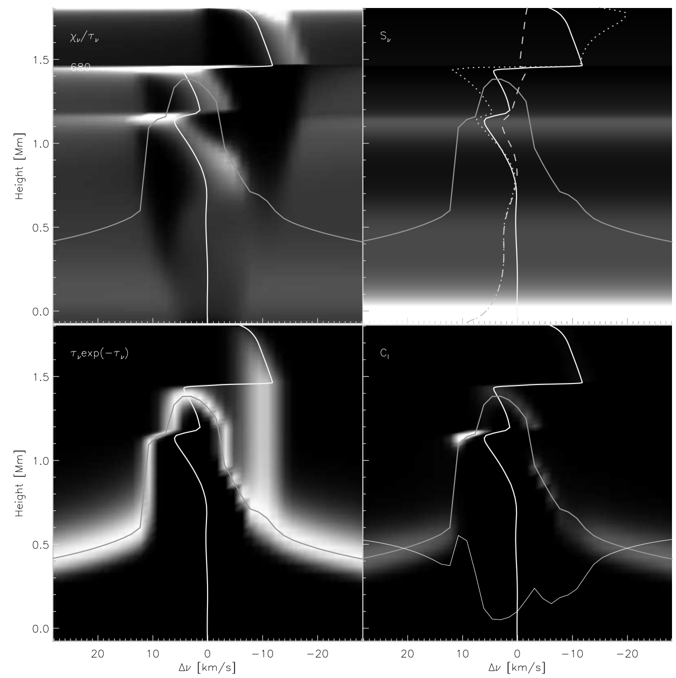

Fig. 7. As Fig. 4 but for t=680s.

due to the overlying downfalling material above the shock.

Figure 6 shows the situation 20 seconds later. The upper wave has become a shock and is about to merge with the top shock. The wave that was at 0.8 Mm has steepened and its amplitude has increased as it moved up to 1 Mm. Due to the non-LTE decoupling, the source function does not increase at the shocks at 1.3 and 1.4 Mm and the dominant maximum in the contribution function is from the wave at 1 Mm that has not quite shocked yet. The blue peak in the emergent intensity at 9 km/s is due to the maximum in the source function produced by the wave at 1 Mm combined with the large χ_ν/τ_ν from 5-10 km/s due to the velocity gradient in this wave and the lack of overlying material with the same velocity.

Figure 7 shows the situation 10 seconds later. The two top shocks have now merged into one and the wave behind is steepening into a shock at 1.2 Mm. The H_{2V} emission comes from 1.2 Mm where both the source function and χ_ν/τ_ν have maxima. The top shock is above the height where $\tau_\nu = 1$ at line center and does not give any emission. The new feature is the red emission peak at -3km/s. The contributions to its intensity come from the regions around 0.9 and 1.3 Mm where χ_ν/τ_ν has maxima to the red of the material velocity because the velocity is decreasing downwards in the wakes of the waves.

3.2. Formation of the grain pattern

We next address the question of what properties of the velocity near $\tau_{500} = 1$ lead to the production of bright grains in Ca II H & K lines in the chromosphere. Explanations in the literature go from very high frequency waves (period on the order of 30s) through the process of shock overtaking (Rammacher & Ulmschneider 1992), three minute waves (Carlsson & Stein 1992), five minute oscillations Kalkofen et al. 1992 to impulse excitation (Kalkofen 1996). To achieve some understanding we have

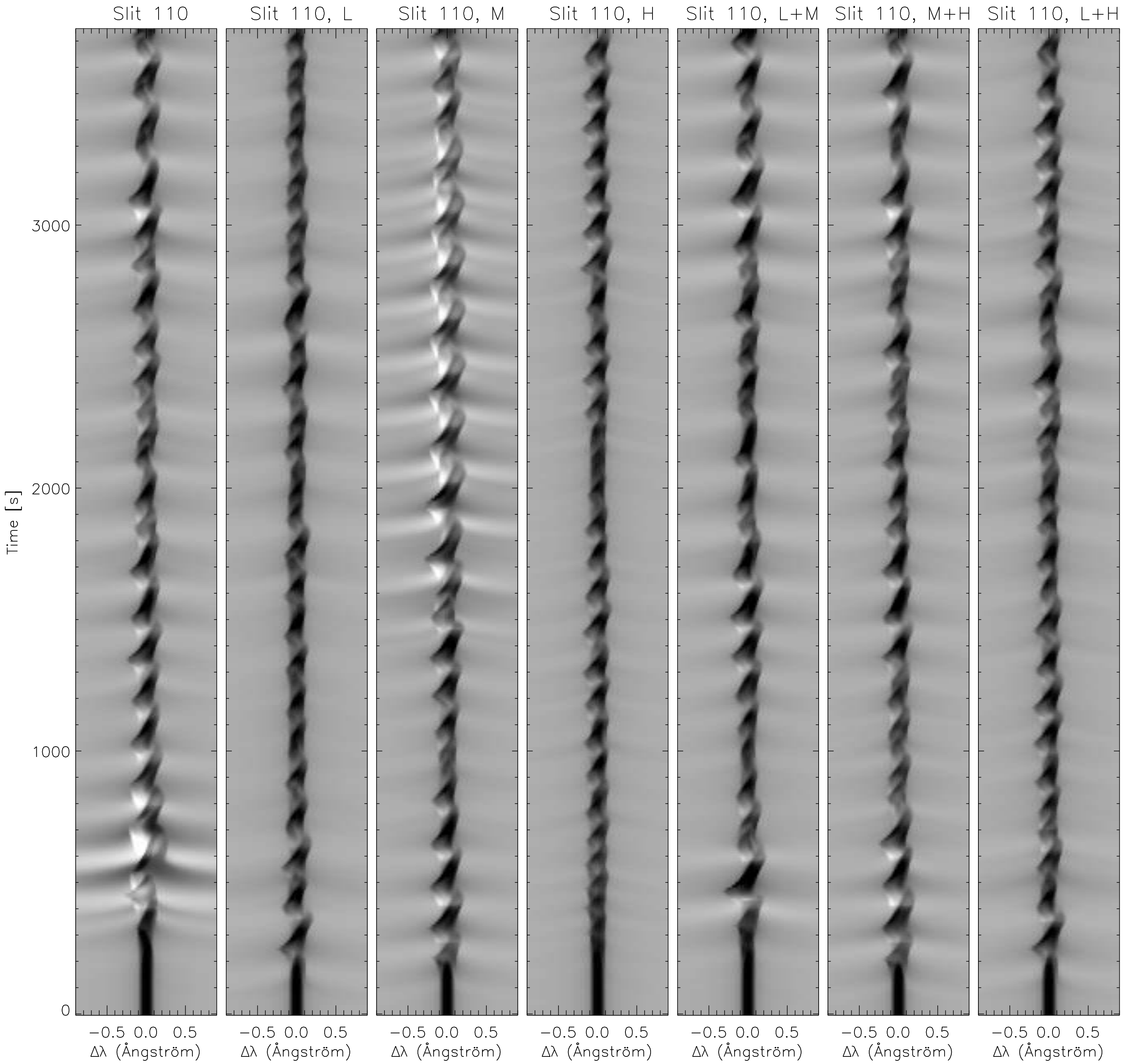

Fig. 8. Intensity as a function of wavelength displacement from line center and time for 7 calculations with different frequency ranges of the piston velocity, all for slit position 110. The full piston velocity spectrum case is compared with those for only Low frequencies ($\nu < 4.7$ mHz), Medium frequencies ($4.7 < \nu < 7.1$ mHz), High frequencies ($\nu > 7.1$ mHz), Low plus Medium ($\nu < 7.1$ mHz), Medium plus High ($\nu > 4.7$ mHz) and Low plus High ($\nu < 4.7$ and $\nu > 7.1$ mHz) respectively from left to right. The bright grain pattern is seen as a brightening in the wings that shift toward the line core with advancing time, followed by a brightening on the blue side of the line core. The full piston spectrum run looks very similar to the medium plus high frequency and the medium plus low frequency cases after the initial startup.

made runs with several different filtered piston velocities, we have looked at velocity and temperature profiles, made Fourier and wavelet transforms and compared all of these.

We have compared the full simulation with simulations where the piston velocity is restricted to certain frequency bands, low (< 4.7 mHz), medium ($4.7 - 7.1$ mHz) and high (> 7.1 mHz) and combinations of these. Intensity as a function of wavelength and time for these simulations corresponding to one slit position are shown in Fig 8.

Runs with only low frequencies ($\nu < 4.7$ mHz) do not produce grains. Thus, the p-mode oscillations near 3 mHz do not contribute to the formation of grains, even though most of the wave power in the photosphere is in this range (Fig 3).

Bright grains are produced by shocks near 1 Mm in the chromosphere (as shown in the previous section 3.1. High frequency waves ($\nu > 7.1$ mHz) produce many shocks and hence grains. However, these grains from high frequency waves rarely coincide with the grains from the runs with the full frequency spectrum of the piston motion (Fig 8), nor with the observed grains (Fig 16). There are always high frequency wave components in the observed Fe line Doppler shift (Fig 3), but these have generally much smaller amplitude than the waves near and below the acoustic cutoff frequency (≈ 5 mHz).

The calculations with piston velocities in the band near the acoustic cutoff frequency, $4.7 < \nu < 7.1$ mHz, produce very strong regular grains (Fig 8), but these look nothing like the full simulation and are likely due to a resonant interaction. It is the interference between mid and high frequency motions in the range $\nu > 4.7$ mHz, that produce the grains observed in the full piston spectrum simulations and that correspond to the observed grains. The calculations with frequencies in the range $\nu > 4.7$ mHz (M+H) and $\nu < 7.1$ mHz (L+M) both have nearly the same grain structure as found in the calculations with the full piston spectrum (Fig 8), except that the L+M run is missing some grains found in the full simulation (e.g. those at 2230 and 2490 s). The addition of either lower or higher frequency components destroys the resonance that exists when only the $4.7 < \nu < 7.1$ mHz waves are present. From these results we conclude that waves near the acoustic cutoff frequency are crucial for producing most grains. These waves are most important because only propagating waves steepen and form shocks, and the photospheric velocity power decreases with increasing frequency, so waves near the cutoff frequency have the largest amplitude. Only a few grains are produced by higher frequency waves.

A different perspective is obtained by studying wavelet transforms. The source function at the height of grain formation (≈ 1.1 Mm) and the velocity (at 1 Mm) have very similar wavelet transforms (Fig 9). For the same slit position as above, there is significant power at the end of the run (> 3000 s) in the band $4 < \nu < 5$ mHz in the source function and $4.5 < \nu < 5.5$ mHz in the velocity. Early in the run (~ 1000 s) there is significant power in both the source function and velocity in the range $5.5 < \nu < 6.5$ mHz. If we follow the velocity wavelet transforms down in height, we see that the $4.5 < \nu < 5.5$ mHz power at the end of the run is from waves whose frequency and interval in time do not change with height. For the higher frequency, $5.5 < \nu < 6.5$ mHz, waves, on the other hand, the peak power at the piston occurs at an earlier time and narrower frequency range ($5.5 < \nu < 6$ mHz) than at 1 Mm. In the middle of the run, $2000 - 2800$ s, the maximum power in the source function occurs at ≈ 7 mHz, but is smaller than the peaks near 1000s and 3000 s. There is no obvious piston velocity power corresponding to this source function power.

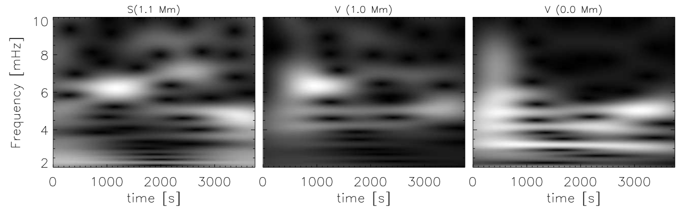

Fig. 9. Wavelet transforms of the source function at 1.1 Mm, in the grain forming region (left), the velocity at 1.0 Mm (center) and the velocity at 0 Mm (right). There is a very close correlation of power between the source function and velocity near 1 Mm. There is large power after 3000 s with $4 < \nu < 5$ mHz in the source function, velocity at 1 Mm and velocity at 0 Mm, corresponding to grains produced by interaction of large amplitude evanescent waves with higher frequencies. There is also large power in the source function and velocity at 1 Mm around 1000 s with $5.5 < \nu < 6.5$ mHz which corresponds to power in the velocity at 0 Mm that stretches from 100 to 1500 s with $5.5 < \nu < 6$ mHz. These are large amplitude waves with frequencies just above the acoustic cutoff frequency.

Further information can be obtained by studying the frequency filtered velocity field as a function of height and time. The band between $4.5 < \nu < 5.5$ mHz (Fig 10) shows large power between 2900 and 3500 s, as expected from the wavelet transform (Fig 9). These waves show very large phase speed and are nearly evanescent. The grains line up with shocks at 3040 and 3470 s. The higher frequency band between $5.5 < \nu < 6.5$ mHz has maximum power between 1000 and 1500 s (Fig 11), consistent with the wavelet results (Fig 9). These waves have a smaller phase speed, but still larger than the sound speed. The grains line up with shocks at 1140, 1310, 1460 and 1630 s. Note, these grains do not line up with the zero crossings of the waves in the lower frequency band, clearly indicating that these lower frequency waves are not responsible for the grains at this earlier time. There are also grains between these two time periods that in general do not line up with the zero crossings of waves in either of these two frequency bands. Grains in the interval $1900 - 2800$ s are due to higher frequency waves, superimposed on top of the stronger waves near the acoustic cutoff frequency (Fig 12). Since grains form at shocks which are high frequency structures, we see all the grains at the zero crossings of shocks in this high frequency range. But, we can trace these high frequency waves back to the piston, where they are small perturbations on larger amplitude medium frequency waves. It is the interaction between them that produces the grains.

Consider some specific examples. The strong grain at 3040 s is due to the interactions between a high amplitude evanescent wave and a high frequency wave that left the piston at 2895 s (Fig 14). This small amplitude, high frequency wave propagates forward on the larger amplitude, evanescent, low frequency wave and produces a shock when it catches up to the crest. This can be seen not only in the filtered velocity images (Fig 12), but also in a time series of velocity and temperature profiles (Fig 13 left). These show only the higher frequency components, since the low frequency evanescent waves are in phase at all heights and not readily visible in this presentation. The grain at 1310 s is due to the interaction of the wave just above the acoustic cut-off with a higher frequency wave that left the piston at 1200 s (Fig 12) and (Fig 13 center). In the piston velocity profile, this high frequency wave shows up as a narrower crest on the long period wave at 1250 s (Fig 14), which makes the crest propagate and steepen more rapidly into a shock than a broader profile would. In contrast, the two grains at 2230 and 2330 s are produced by high frequency waves that leave the piston in the trough of longer period waves at 2080 and 2150 s (Fig 12) and (Fig 13 right). Note in the piston velocity profile (Fig 14), these are individual peaks that have significant amplitude compared to the larger amplitude lower frequency waves existing at the same time. These grains are absent in the low plus medium ($\nu < 7.1\,\mathrm{mHz}$) run (Fig 8).

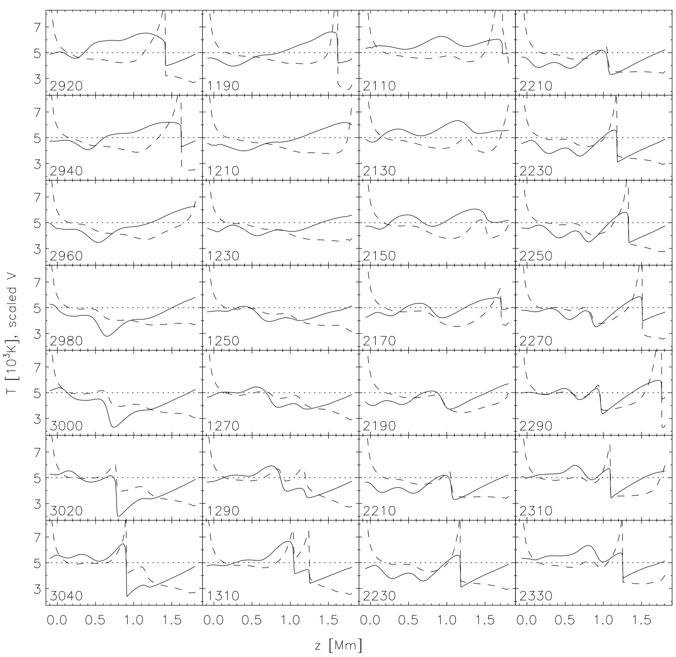

Fig. 13. Velocity (solid) and temperature (dashed) profiles with height at 20 s intervals. The velocity is scaled by $\rho_o^{1/4}$ and the dotted line is zero velocity. The temperature is shown in units of 10^3 K. The bottom row shows the state at the time of grain occurence.
[Left] Formation of the bright grain at 3040 s from a high frequency wave generated by the piston at 2895 s that interacts with a large amplitude low frequency wave whose crest is produced by the piston at 3030 s.
[Center] Formation of the bright grain at 1310 s from a high frequency wave generated by the piston at 1200 s that narrows the crest of the longer wavelength, low frequency wave on which it rides that leaves the piston at 1250 s. The grain is produced by the lower, not the higher shock, because it occurs at a higher density. These two shocks merge shortly after the grain is produced, but by then they are at too low a density to produce a grain.
[Right 2 columns] Formation of the bright grains at 2230 and 2330 s produced by high frequency waves generated by the piston at 2085 and 2150 s. Longer wavelength, low frequency waves are weak during this time interval.

Previous history of the atmosphere has also been considered a possible explanation for grain formation. We investigated the importance of the piston velocity pattern versus the previous

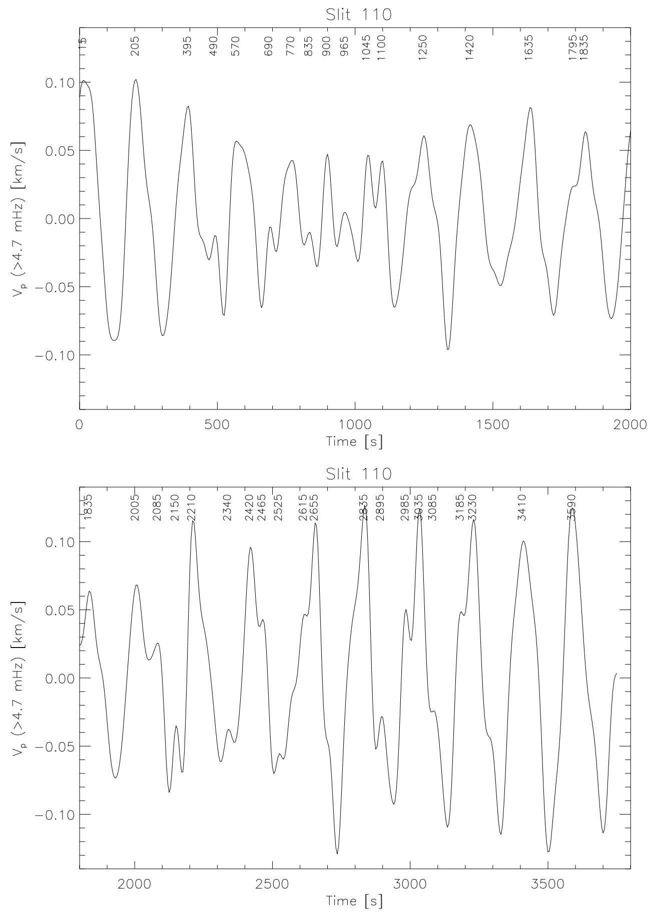

Fig. 14. The velocity profile of the piston as a function of time. The velocity shown has been filtered to remove frequencies < 4.7 mHz, so that only waves that contribute to grain formation are displayed.

history of the atmosphere by performing a simulation with a 3750 second piston velocity sequence repeated twice. The piston velocity at t=3750+t_0 is thus identical to the piston velocity at t=t_0. The resulting H-profile as a function of time is shown in Fig. 15. The time evolution has been split into two panels with the right panel showing the second half of the simulation. The piston velocity is thus the same at the same vertical position in the two panels. It takes some time for the initial waves to reach the line forming regions, which is why there is no change with time in the beginning. The beginning of the second half of the simulation is also atypical since there is a sudden phase jump when the velocity pattern restarts. Outside these startup periods, the two halves of the simulation show almost exactly the same grain development with no pronounced grains in the time intervals 900–1450s and 4650–5200s and strong grains in the time intervals 1450–2600s and 5200–6350s. We conclude that there is no long time memory in the atmosphere and that the bright grain pattern is completely determined by the velocity pattern in the photosphere.

Shock merging of high frequency waves has also been proposed as the mechanism for grain formation. As can be seen in Figs 12 and 13, shock merging is involved in the formation of about half the grains, but the other half are entirely due

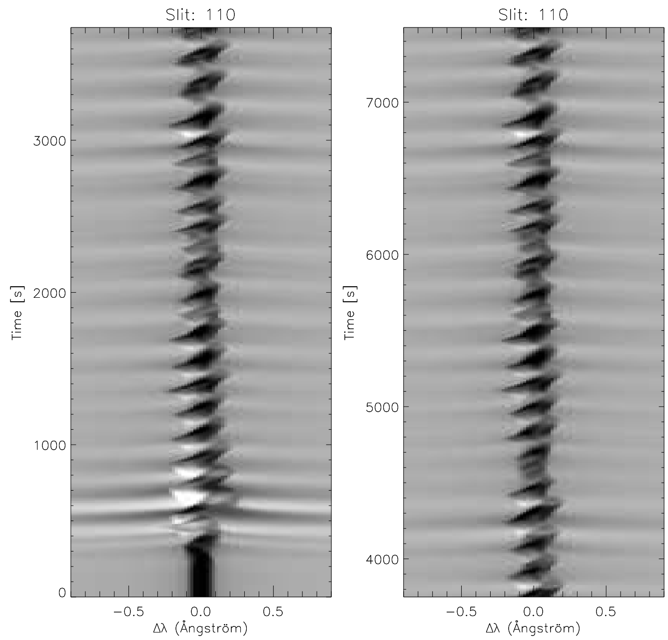

Fig. 15. The computed Ca II H line intensity as a function of wavelength for a simulation where the piston velocity repeats after 3750 s. The two panels are for the two halves of the run, so that one vertical position in the two panels have the same piston velocity. The pattern is almost identical in the two sections of the simulation outside the first startup periods.

to isolated shocks. Shock merging is an incidental event in the process of bright grain formation.

Thus, bright grains are produced by powerful waves near or just above the acoustic cutoff frequency interfering with higher frequency waves that induce them to steepen rapidly, or by high frequency waves acting on their own when waves near the acoustic cutoff frequency are weak. It is difficult to predict when grains will form from such high frequency waves, since they are always present. But where there is significant power around 5 mHz (3 min period), there will usually be significant grains. The trapped p-modes near 3 mHz (5 min period) do not lead to the formation of bright grains.

3.2.1. Comparison with observations

We made simulations with piston velocities chosen to reproduce the measured Doppler shifts in the iron line at 396.68 nm at four different slit positions in the observations by Lites et al. (1993). Fig. 16 compares the computed behavior of the H line with these observations for two different slit positions. At the beginning of the simulation there are startup effects clearly visible for slit position 110 up to about 1000s. After this startup period there is a general correspondence between the simulations and the observations down to the level of individual grains. The simulations show the characteristic behavior of H_{2V} grains: a brightening in the wings that propagates toward line center and creates a bright grain when reaching a wavelength of about -0.1 Å. The dark line core moves slowly to the red and then, just after the appearance of the grain, abruptly to the blue. Many individual grains are well reproduced: at slit position 110 the strongest observed grains are at t=1460, 1605, 1815 and 3015s. These correspond to grains in the simulations at t=1460, 1630, 1800 and 3040s. Other grains are stronger in the simulations than in the observations, notably at t=1310s. The same good correspondence is found between the simulations and the observations at slit position 132 (Fig. 16, right panels).

The simulations for slit positions 149 and 30 show less good agreement with the observations (Fig. 17). The qualitative agreement for slit position 149 is good but the grains are brighter and there are grains in the simulations that are not seen in the observations, especially after t=2000s. This is even more pronounced at slit position 30 where the bright grains in the simulations at t=2010, 2140 and 2270 s are not seen in the observations. From a detailed study of the formation of these grains using the techniques discussed in Section 3.2 it is clear that these grains are strongly influenced by waves with frequencies near 7 mHz that grow abnormally due to a resonance phenomenon. The three bright grains at slit position 30 can be traced back to a 14 mHz wave-train of high amplitude at t=1870-2130 s, which is a time of low power in the 4.5–6 mHz range. In times of low power close to the acoustic cut-off frequency, it seems the simulations exaggerate the influence of high frequency waves. This could be due to the neglect in our 1D approximation of interfering high frequency waves from other spatial points. Such interference would be more important for high frequency waves with short wavelength than for the waves close to the acoustic cut-off frequency, which propagate more vertically. Another possible explanation is that the observed Doppler-shifts in the iron line contain too much high frequency power due to effects of seeing and large gradients in line-of-sight velocity on the Sun close to slit position 30.

Different photospheric velocity patterns observed at different slit positions thus give rise to very different bright grain patterns produced by acoustic shocks in the mid-chromosphere and these generally agree with the observed grain pattern at those positions. There is a distribution of time intervals between the appearance of grains at a given location which is peaked near the acoustic cutoff period of 3 min, as is found in the observations (Von Uexkuell & Kneer 1995). There is no need to invoke channeling by magnetic fields to obtain intermittent small sized grains. Their size and time of appearance are completely controlled by the photospheric velocity field, which is probably due to the interference of very many p-modes with frequencies near and larger than the acoustic cutoff frequency.

The general agreement gives some confidence that the simulations describe the physical processes most important for the bright grain phenomenon. What are the important *discrepancies* between the simulations and the observations and what can be learned from them? The simulations show a much larger contrast with a sharp transition to a very dark, rather flat core region. There are more details in the dark core region with frequent secondary maxima. It is possible that the observed line core is brighter than in the simulations because of the existence of a hotter magnetic region in the line core forming layers, which lie above the bright grain forming layers by several hundred kilometers. Some of this discrepancy could also be due to observational effects. Limited instrument resolution will cause a smearing in the wavelength domain. Scattered light in the instrument decreases the contrast and mixes in signal from other spatial positions on the sun. Seeing further widens the

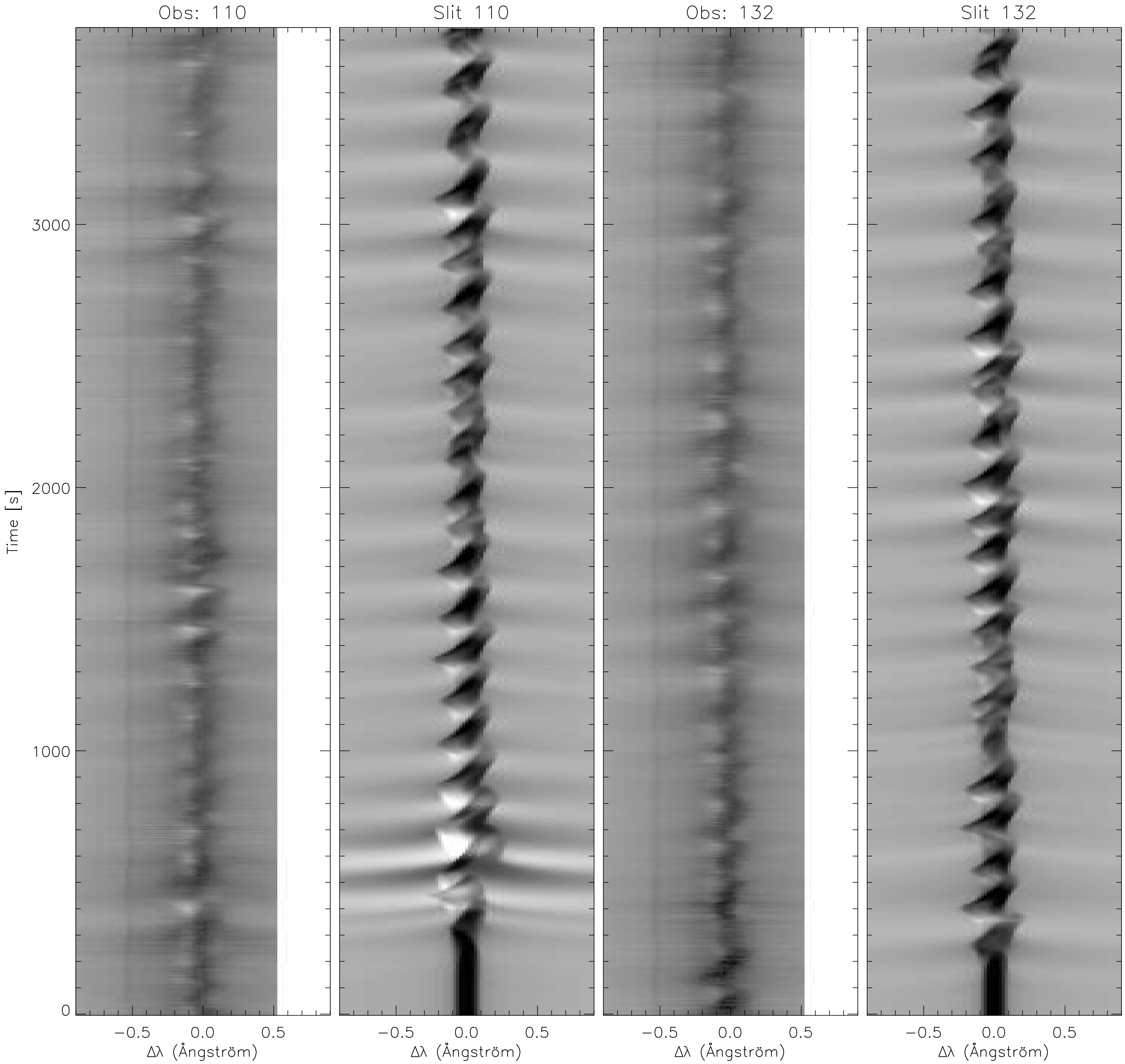

Fig. 16. The computed Ca II H line intensity as a function of wavelength and time compared with observations for slit positions 110 and 132. There is a close correspondence between the simulated and observed grains after the initial startup period.

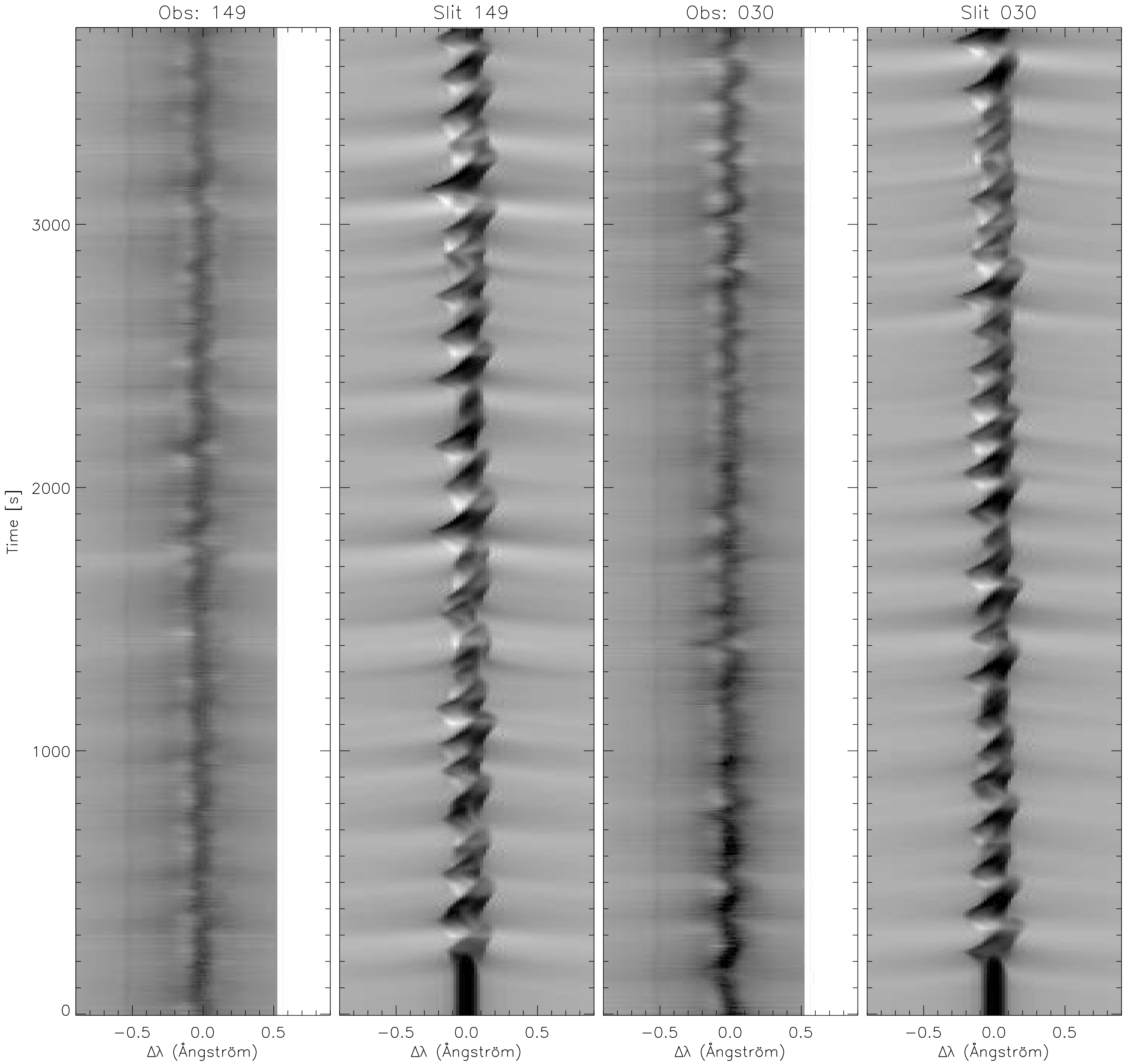

Fig. 17. The computed Ca II H line intensity as a function of wavelength and time compared with observations for slit positions 149 and 30. Some grains in the simulations are not seen in the observations.

total point spread function and also introduces signal from more distant spatial points through image motion.

It is almost impossible to remove these effects from the observations since the various convolutions are poorly known. A difficulty with including these effects in 1-D simulations is the unknown spatial correlation. In lieu of a detailed study, we illustrate the effects to be expected by showing the simulation with various degrees of smearing in Fig. 18. Spatial smearing has been simulated by a smearing in the time domain. Note that the simulated image motion introduces intensity variations coherent in wavelength (horizontal bands) that can also be seen in the observations. It is clear that the difference in the form of the profile and in contrast may be due to observational effects. To obtain the maximum information content in the observations one thus has to spend a lot of effort on minimizing scattered light and effects of smearing by seeing.

Another difference with observations is a difference in the time when the grains appear. The simulated grains come between 25 s earlier and 25 s later than the observed grains for slit position 110, with an average close to zero. For slit position 132, on the other hand, the simulated grains come systematically later than the observed grains by between 15 and 40 s. These phase differences are, however, close to the phase differences between the simulated velocity at 260 km height and the observed Doppler shifts in the iron line at 396.68 nm in the frequency range 4.5 – 7 mHz (Fig. 3). We conclude that the differences in time of the grains are due to the inadequacy of our transfer function to reproduce the observed velocity field in the photosphere.

The inner wings of the Ca II H-line are brighter in the simulations than the observations and the grains are substantially brighter. Both the peak intensity and the inner wing intensity is expected to be lower in partial redistribution (PRD) than in CRD (e.g. Shine et al. 1975). A detailed comparison of the line profile would thus have to take into account the effects of PRD on the profile.

To summarize: the observed grain occurrences are generally well reproduced by the calculations. The simulated grain appearance differs from that observed by having too dark line cores and too bright grains and inner wings. Some of these differences between the calculations and the observations are likely due to seeing effects. Others are due to the limitations in the calculation, which are discussed in the next section.

4. LIMITATIONS

Maybe the most important limitation of the simulations is the 1D restriction of horizontal homogeneity. The energy is forced to travel vertically, there is no radiative loss horizontally and there is no interference between velocities from different spatial points. All these effects can be expected to be important to the physics of the solar chromosphere. The observed spatial extent of bright grains is a few arcseconds similar to the total vertical extent of the simulation. A 1D description can therefore be expected to show some resemblance to the real sun, a view supported by the close resemblance of the simulations to observations of high spatial resolution. We thus feel that we can learn something about the real sun from the simulations but warn against over-interpretations.

The simulations aim at describing the non-magnetic internetwork regions of the sun. At some height this distinction between non-magnetic and magnetic regions has to break down with the spreading of the magnetic fields. Such a canopy has not been included in the simulations and for large heights one has to be increasingly careful of comparisons with observations. Hot material contained in magnetic regions above the internetwork may influence the non-magnetic regions we aim at simulating by modifying the line core source function and reflecting waves.

Line-blanketing was neglected in our simulations. This affects the temperature structure in the upper photosphere in the initial model and therefore the H line wing intensities. Inclusion of line-blanketing would also increase the radiative damping in the upper photosphere and low chromosphere and so decrease the growth of wave amplitudes in that height range. The inclusion of cooling from CO, Mg h & k, and other coolants that we have neglected in the simulation would have similar effects. The brightness of the grains is sensitive to the height of shock formation. Smaller amplitude waves will shock at greater heights and produce weaker grains, in better agreement with observations.

Complete redistribution (CRD) has been assumed for all transitions. The Ca II H and K profiles will be affected by the neglect of partial redistribution (PRD). A proper PRD treatment would involve angle dependent redistribution. PRD will lower the intensity of both the grains and the inner wings. Details in the computed profiles, especially peak intensities and the inner wing intensity, should therefore be treated with caution.

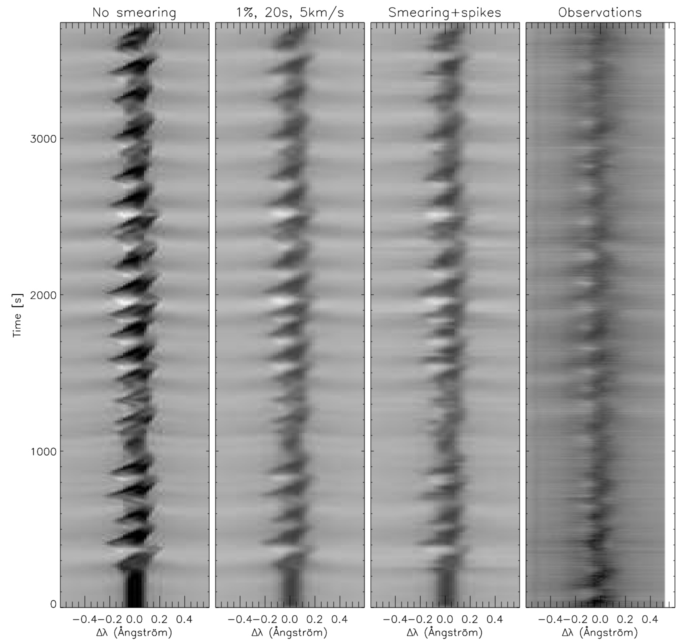

Fig. 18. The computed Ca II H line intensity at slit position 132 as a function of wavelength and time compared with observations. The leftmost panel shows the unsmeared results from the simulation. In the second panel the simulation has been convolved with a Gaussian point spread function with FWHM of 20 seconds in the time domain and 0.066 Å (corresponding to 5 km/s) in the wavelength domain. Scattered light amounting to 1% of the continuum intensity has been added. In the third panel image motion has been simulated by shifting the sequence in time with a random function. The same smearing and scattered light as in the second panel was also added.

The limited numerical resolution will especially affect higher frequencies. The adaptive grid moves grid-points into shock regions but the resolution of waves starting to develop is limited. At the height of the piston the distance between grid-points is 1 km, increasing to 20 km above 300 km height. With ten points per wavelength, this corresponds to a 30 mHz maximum frequency for waves that are resolved everywhere, so the numerical resolution should not much affect the high frequency waves before they start to shock.

The upper boundary condition aims at being transparent. During the timespan of the simulation, significant mass flows out of the boundary (4×10^{-4} g cm^{-2} over 7500 seconds). This has been taken into account by increasing the column mass of the top point correspondingly but no effect has been included on the pressure. The mass above the computational domain is thus not supported by the atmosphere in the simulation. The outflow matter is also assumed to be transparent; no additional opacity is added in.

5. CONCLUSIONS

The simulations closely match the observed behavior of Ca II H_{2V} bright grains down to the level of individual grains. There are several significant differences, however, which gives us important information on where the theory and the observations need to be improved. The occurrence time of the simulated grains is different than the observed grains by a few tens of seconds. This seems to be due to imperfections in the transfer function, so that the velocities do not match the observed iron line Doppler shifts sufficiently accurately. The simulated grains are stronger than the observed grains, even after smoothing to represent seeing effects. This may be due to the 1D plane wave nature of the calculation, to the neglect of partial redistribution, to neglect of important coolants, or to seeing. The simulated line cores are darker than the observations. This may be due to effects of scattered light on the observations, or to the existence of a hotter magnetic region in the line core forming layers which lie above the bright grain forming layers by several hundred kilometers. Finally, the grains produced primarily by high frequency waves in the simulation are often absent in the observations. Their presence in the simulations may be due to the 1D nature of the calculation, so that these high frequency waves to not spread horizontally, it may be due to the resonance that occurs in the calculation, or it may be due to excess power in the iron line observations at high frequencies because of image motion and seeing effects.

The bright grains are produced by shocks near 1 Mm above $\tau_{500}=1$. Shocks in the mid chromosphere produce a large source function (and therefore high emissivity) because the density is high enough for collisions to couple the Ca II populations to the local conditions. The asymmetry of the line profile is due to velocity gradients near 1Mm. Material motion Doppler shifts the frequency where atoms emit and absorb photons, so the maximum opacity is located at – and the absorption profile is symmetric about – the local fluid velocity, which is shifted to the blue behind shocks. The optical depth depends on the velocity structure higher up. Shocks propagate generally into downflowing material, so there is little matter above to absorb the blue Doppler shifted radiation. The corresponding red peak is absent because of small opacity at the source function maximum and large optical depth due to overlying material. The brightness of the violet peak depends on the height of shock formation. The lower the shock, the higher the density and the larger the source function. The position in wavelength of the bright violet peak depends on the bulk velocity at the shock peak and the width of the atomic absorption profile (described with the microturbulence fudge parameter).

The bright grains are produced primarily by waves near and slightly above the acoustic cutoff frequency. The precise time and strength of a grain depends on the interference between these waves at the acoustic cutoff frequency and higher frequency waves. When waves near the acoustic cutoff frequency are weak, then higher frequency waves produce grains. The "five-minute" trapped p-mode oscillations are not the source of the grains, although they can modify the behavior of higher frequency waves. The wave pattern that exists at the solar surface is due to the interference of many trapped and propagating p-modes, so that the grain pattern repeats over short time intervals but has a stochastic nature over long time periods.

Lites and Rutten are thanked for making available their observations. This work was supported by a grant from the Norwegian Research Council and by grant NAGW-1695 from the National Aeronautics and Space Administration. The computations were supported by a grant from the Norwegian Research Council, tungregneutvalget.

REFERENCES

Carlsson, M. 1986, Report No. 33, Uppsala Astronomical Observatory
Carlsson, M., Stein, R. 1992, ApJ, 397, L59
Carlsson, M., Stein, R. F. 1995, ApJ, 440, L29
Dorfi, E. A., Drury, L. O. 1987, J. Comput. Phys., 69, 175
Gustafsson, B. 1973, Uppsala Astr. Obs. Ann., 5, No. 6
Hofmann, J., Steffens, S., Deubner, F. L. 1996, A&A, 308, 192
Kalkofen, W. 1996, ApJ, 468, L69
Kalkofen, W., Rossi, P., Bodo, G., Massaglia, M. 1992, in M. S. Giampapa, J. A. Bookbinder (eds.), Seventh Cambridge Workshop on Cool Stars, Stellar Systems and the Sun, Astron. Soc. Pac. Conf. Series, Vol. 26, p. 543
Lites, B. W., Rutten, R. J., Kalkofen, W. 1993, ApJ, 414, 345
Rammacher, W., Ulmschneider, P. 1992, A&A, 253, 586
Rossi, P., Kalkofen, W., Bodo, G., Massaglia, S. 1992, in M. Giampapa, J. M. Bookbinder (eds.), Cool Stars, Stellar Systems and the Sun, Proc. Seventh Cambridge Workshop, Astron. Soc. Pac. Conf. Series, in press
Rutten, R. J., Uitenbroek, H. 1991, Solar Phys., 134, 15
Scharmer, G. B. 1981, ApJ, 249, 720
Scharmer, G. B., Carlsson, M. 1985, J. Comput. Phys., 59, 56
Shine, R. A., Milkey, R. W., Mihalas, D. 1975, ApJ, 199, 724
Steffens, S., Hofmann, J., Deubner, F. L. 1996, A&A, 307, 288+
van Leer, B. 1977, J. Comput. Phys., 23, 276
Von Uexkuell, M., Kneer, F. 1995, A&A, 294, 252